

# Atomic Force Microscopy Capable of Vibration Isolation with Low-stiffness Z-axis Actuation

Shingo Ito, Georg Schitter

*Automation and Control Institute (ACIN), TU Wien, Gusshausstrasse 27-29, 1040 Vienna, Austria  
(email: {ito, schitter}@acin.tuwien.ac.at)*

---

## Abstract

For high-resolution imaging without bulky external vibration isolation, this paper presents an atomic force microscope (AFM) capable of vibration isolation with its internal Z-axis (vertical) actuators moving the AFM probe. Lorentz actuators (voice coil actuators) are used for the Z-axis actuation, and flexures guiding the motion are designed to have a low stiffness between the mover and the base. The low stiffness enables a large Z-axis actuation of more than  $700\text{ }\mu\text{m}$  and mechanically isolates the probe from floor vibrations at high frequencies. To reject the residual vibrations, the probe tracks the sample by using a displacement sensor for feedback control. Unlike conventional AFMs, the Z-axis actuation attains a closed-loop control bandwidth that is 35 times higher than the first mechanical resonant frequency. The closed-loop AFM system has robustness against the flexures' nonlinearity and uses the first resonance for better sample tracking. For further improvement, feedforward control with a vibration sensor is combined, and the resulting system rejects 98.4% of vibrations by turning on the controllers. The AFM system is demonstrated by successful AFM imaging in a vibrational environment.

**Keywords:** Atomic force microscopy, Vibration isolation, Voice coil actuators, Robust control

---

## 1. Introduction

To investigate sample properties with high resolution, atomic force microscopes (AFMs) have a sharp probe that is scanning over the sample surface while the Z-axis (vertical) position of the probe is controlled to maintain the tip-sample distance or the probe deflection with nanometer resolution [1]. Due to the required positioning resolution, AFMs are usually sensitive to external disturbances [2]. Particularly floor vibrations, typically generated by people on the floor and traffic around the building [3], influence the designs and specifications of AFMs.

Floor vibrations can excite mechanical resonances of AFMs and fluctuate the probe's Z-axis position, resulting in artifacts on AFM images [4]. In the case of rigid AFMs, this problem is solved by increasing their resonant frequencies sufficiently higher than the floor vibrations' major spectrum [5]. For this purpose, rigid AFMs must have a rigid and short mechanical loop between the AFM probe and the sample [2, 5]. Because the mechanical loop includes the Z-axis actuator of the probe, commonly used piezoelectric actuators are ideal with their high intrinsic stiffness for the loop rigidity. Due to the high stiffness, however,

*Preprint submitted to Ultramicroscopy*

*October 19, 2017*

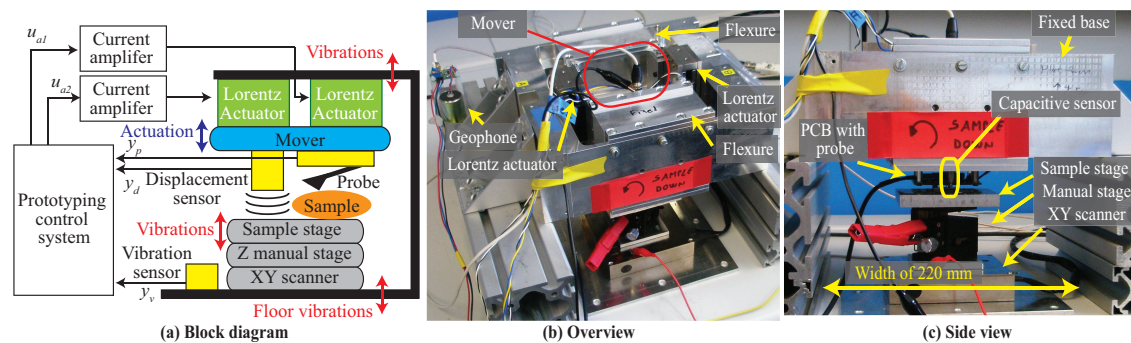


Figure 1: AFM system showing (a) block diagram, (b) photographs of overview and (c) side view.

the Z-axis stroke of the probe is strictly limited, and a sample with high topography cannot be imaged [6]. The rigid design also limits the sample width for the short mechanical loop [5, 7], which is a problem with wide samples (e.g. petri dishes and wafers [2]). Furthermore, the rigid design poses additional challenges for the design of user-friendly automated AFMs. Motorized stages for the coarse positioning of the sample or for the probe engagement are relatively large and heavy in the mechanical loop. Thus, they can result in low-frequency resonances to be excited by floor vibrations [8].

In comparison to rigid AFMs, typical AFMs with a larger actuation range have mechanical resonances at lower frequencies. For high quality imaging, they are typically operated in a quiet room, ideally satisfying certain standards (e.g. Vibration Criterion (VC) [9]). In addition, AFMs are usually placed on the tabletop of an external vibration isolator. Even with such an isolator, however, the mechanical resonances of AFMs are desired to be more than several tens of Hertz because isolating floor vibrations is difficult at low frequencies. In the case of passive vibration isolators (e.g. optical tables), their tabletop supports mechanically transmit floor vibrations below the first resonant frequency [10]. In the case of active vibration isolators, the signal-to-noise ratio of their vibration sensors degrades at low frequencies [11], and floor vibrations cannot be isolated [12]. Consequently typical AFM systems are heavy and bulky with an external vibration isolator, and they have to be placed in a quiet environment.

Overall, the vibration sensitivity of AFMs is a weakness, restricting the sample size, the functionality, and the suitability of operation sites. However, fully automated AFMs are desired to be operated in vibrational environments, with a large sample, and without external vibration isolation for compactness. The applications include AFM imaging in a production line for inline metrology [13] and on-site AFM imaging, such as imaging of marine bacteria [14] on a boat or fossils [15] in a vehicle during field trips. In addition to the vibration sensitivity, AFMs usually have a design trade-off to determine the Z-axis actuator's stiffness between the achievable Z-axis stroke and the closed-loop control bandwidth. A high stiffness is desired for a high bandwidth. This is because the bandwidth is typically restricted by the actuator's first resonant frequency [16], which can be higher by increasing the stiffness. In return, the high stiffness decreases the achievable stroke for a given actuation force. In this stiffness dilemma, the Z-axis stroke and the bandwidth are adjusted by selecting actuators and by designing the actuator flexures [17].

To enable inline metrology and on-site imaging, this paper proposes an AFM system ca-

pable of vibration isolation for imaging without external vibration isolation. The proposed AFM system uses flexure-guided Lorentz (voice coil) actuators for the probe's Z-axis actuation. They have a low stiffness between the mover and stator such that vibrations transmitted to the probe are mechanically isolated at high frequencies. The residual vibrations are detected by a displacement sensor monitoring the probe-sample distance [4, 18, 19], and they are rejected by the Z-axis actuators with feedback control. Its closed-loop control bandwidth is significantly higher than the first resonant frequency, overcoming the stroke-bandwidth trade-off. As a feasibility study, this paper focuses on the vibration isolation along the Z axis.

This paper is organized as follows. Section 2 describes the vibration isolation concept and the proposed AFM system. Its mechanical design is presented and analyzed in Section 3. In Section 4 the system is modeled, for control design in Section 5. The vibration isolation is demonstrated and evaluated by AFM imaging in Section 6, while Section 7 concludes the paper.

## 2. System description

### 2.1. Vibration isolation concept

The proposed AFM system is illustrated in Fig. 1(a), the floor vibrations oscillate the sample and the mover with the AFM probe differently due to a relatively long mechanical loop from the sample to the probe. The mover and the probe are vertically moved by the Z-axis actuators guided by flexures with lowered stiffness. The low stiffness is beneficial to better decouple the mover with the probe from the actuator stator, which mechanically isolates the vibrations from the stator at frequencies sufficiently higher than the first resonance, in the same manner as passive vibration isolators [10]. The low stiffness is also desired for a large actuation range, as well as for low power consumption in the case of actuation with an offset. To reject the residual probe vibrations and the sample vibrations, the actuators maintain the Z-axis distance between the probe and the sample. Feedback control is used with a displacement sensor measuring the probe-sample distance. Because such a sensor has a high signal-to-noise ratio even at DC [20], the AFM system can reject vibrations at low frequencies, unlike active vibration isolators. The vibration rejection is further improved by using feedforward control [12] with a vibration sensor that measures the floor vibrations. The measured floor vibrations are used to estimate the resulting change in the probe-sample distance, based on which feedforward control moves the mover for vibration cancellation.

To sufficiently decrease the actuator stiffness, Lorentz actuators are selected as the Z axis actuators because they do not add a stiffness between the mover and stator, unlike piezoelectric actuators. The flexure-guided Lorentz actuators are designed such that the second resonant frequency is significantly higher than the first resonant frequency. By doing so, the closed-loop control bandwidth can be significantly higher than the first resonance, overcoming the stroke-bandwidth trade-off of the Z-axis actuation. Such an actuation system is categorized as “low-stiffness actuators” [21] and can achieve nanometer positioning resolution even without external vibration isolation [22]. Note that low-stiffness actuators can be used for vibration isolation in addition to the Z-axis actuators of AFMs as a dual stage actuator [23]. However, the additional actuators need their own amplifiers, introducing additional positioning noise. Furthermore, the vibration isolation of the additional actuators can be

impaired by the recoil of the Z-axis actuators. Thus, it is desired to isolate vibrations only by using the Z-axis actuators.

In the case of conventional AFMs, the first resonant frequency of the Z-axis actuators is usually close to the higher resonant frequencies, whether piezoelectric [24] or Lorentz actuators [6, 25, 26] are used. This is a problem to achieve a closed-loop control bandwidth beyond the first resonant frequency due to the difficulty to assure a sufficient stability margin [21]. Although the bandwidth can be increased by using a displacement sensor, it is still limited by the first resonance [27]. The following design presents that the Z-axis control bandwidth can be significantly higher than the first resonance by selecting Lorentz actuators [21] and properly designing a mechatronic system. The achieved high bandwidth is utilized especially for AFM imaging in a vibrational environment in this paper.

## 2.2. System architecture

Fig. 1(b)(c) shows photographs of the proposed AFM system. Two Lorentz actuators (AVA 2-20, Akribis Systems, Singapore) are used, providing sufficient force for the Z-axis actuation. To reduce the mover weight for a high control bandwidth, the actuators' relatively heavy magnets are stiffly connected to the fixed base while the Lorentz coils are attached to the mover. Because the Lorentz force is proportional to the coil current, the Lorentz actuators are driven by custom-made current amplifiers.

As the displacement sensor on the mover, a capacitive displacement sensor (6810(6504-01), MicroSense, Lowell, USA) is selected for its compact size, high resolution and high bandwidth [20]. The sensor has a measurement range of  $100\text{ }\mu\text{m}$  and a bandwidth of 20 kHz. The measured root-mean-square (RMS) noise is 5.88 nm, from which its PSD is calculated as  $0.042\text{ nm}/\sqrt{\text{Hz}}$  by assuming that the noise is white Gaussian. When the distance to the sample is directly measured by a compatible sensor, the sample can be as large as 220 mm due to the large space under the mover (Fig. 1(c)). To focus on the demonstration of the vibration isolation in this paper, however, the displacement sensor measures the distance between the mover and the sample stage.

A thick aluminum plate ( $63 \times 80 \times 10\text{ mm}$ ) is used as the sample stage to prevent its deformation and placed on a manual stage for the coarse Z-axis adjustment. These stages are mounted on a piezoelectric XY scanner (NPXY100-100, nPoint, Middleton, USA) for scanning the AFM sample. For environmental evaluation and feedforward control, a geophone (SM-7/U-B(10Hz), ION, Houston, USA) is mounted as the vibration sensor on the fixed base with a preamplifier that provides a constant sensitivity approximately between 10 Hz and 340 Hz (Fig. 1(b)).

An Akiyama probe (A-PROBE-10, Nanosensors, Neuchatel, Switzerland) is used as the AFM probe in the constant height mode [2] to evaluate the vibration isolation for imaging. It is a self-sensing and self-actuating probe using a quartz tuning fork [28] and oscillates at its resonant frequency of about 45 kHz, which varies dependent on the distance between the sharp tip and the sample. For the tip-sample-distance measurement, a PCB is implemented and attached to the backside of the mover. The probe has a sensitivity of  $K_{ps} = 1.56\text{ V}/\mu\text{m}$  for AFM imaging within a range of about 400 nm. The measured RMS noise with a 10 kHz low-pass filter is 1.17 nm. The vertical position of the displacement sensor is adjusted on the mover with respect to the probe such that both sensors are within their measurement range. There is a horizontal distance of 20 mm between the probe and the displacement

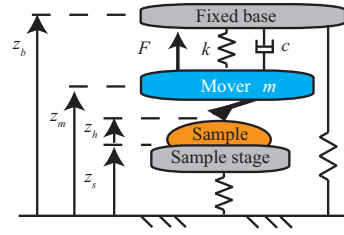


Figure 2: Lumped mass model of the AFM system.

sensor (Fig. 1(a)). The mass of the mover is about  $m = 0.86$  kg, including the displacement sensor, the Lorentz coils and the AFM probe's PCB.

As shown in Fig. 1(a), the current amplifiers, the displacement sensor and the AFM probe's PCB are all connected to a rapid prototyping control system (DS1005, dSPACE GmbH, Paderborn, Germany), where controllers are implemented at a sampling frequency of  $f_s = 20$  kHz. In Fig. 1(a),  $y_p$  represents the output of the AFM probe's PCB while  $y_v$  and  $y_d$  are the outputs from the vibration and displacement sensors, respectively. The proposed AFM system can be illustrated by a lumped mass model in Fig. 2, where  $k$ ,  $c$ , and  $F$  are the overall stiffness, damping and force of the flexure-guided Lorentz actuators, respectively. The other springs represent parasitic dynamics. The vertical position of the mover is denoted by  $z_m$ . While  $z_b$  and  $z_s$  are the position of the fixed base and the sample stage,  $z_h$  is the sample height including features to be imaged.

The AFM system is placed on a standard laboratory table without external vibration isolation for AFM imaging. For the development and analysis of the AFM system, floor vibrations are evaluated by the geophone on the laboratory table (cf. [23]). The vibrations are mainly up to about 150 Hz, with large components below 30 Hz. According to the VC criteria [9], the environment has a vibration level of VC-B, which is not suitable for high-resolution imaging.

### 3. System design and analysis

This section presents the detailed mechanical design and analysis of the proposed AFM system to isolate and reject the floor vibrations measured in the previous section.

#### 3.1. Flexure design

As a compact mechanical guide, leaf-spring flexures (i.e. flat springs) are selected for the AFM system because they can realize relatively low stiffness [17], which is ideal for constructing low-stiffness actuators [29]. For simplicity of manufacturing, all leaf-spring flexures are identical with a uniform cross section and are manufactured from aluminum sheets.

By assuming that the flexure damping and mass are sufficiently small, the first resonant frequency of the AFM system can be approximated by its natural frequency[29]

$$\omega_n = \sqrt{\frac{k}{m}} = \sqrt{\frac{n_{flex} E w_{flex} h_{flex}^3}{m L_{flex}^3}}, \quad (1)$$



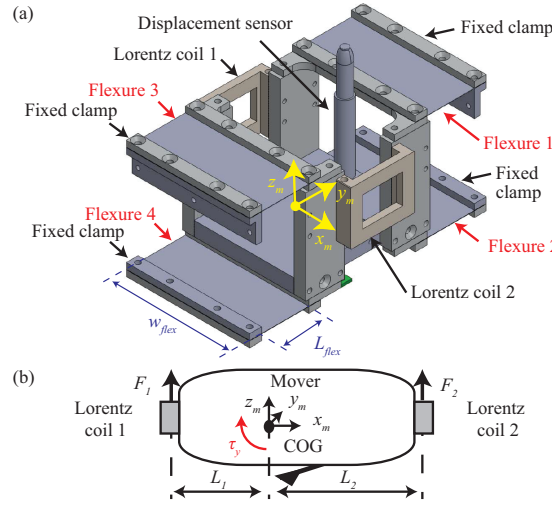


Figure 3: Mover guided by the flexures: (a) 3D model and (b) conceptual cross-sectional view with a coordinate frame at its center of gravity. The Lorentz coil 1 and 2 exert force  $F_1$  and  $F_2$ , respectively, creating a torque  $\tau_y$  around the  $y_m$  axis.

where  $n_{flex}$  and  $E$  are the number of the flexures aligned in parallel and the Young's modulus of the aluminum (68 GPa), respectively. The parameters  $L_{flex}$ ,  $w_{flex}$ ,  $h_{flex}$  denote the length, width and height of a single flexure, respectively, as shown in Fig. 3(a).

In the case of conventional AFMs, the first mechanical resonance is usually regarded as an undesired property, restricting the control bandwidth [25, 26]. In contrast, the proposed AFM uses the first resonance to increase the open-loop gain for the improvement of the vibration rejection in feedback control design (Section 5.1). To efficiently utilize the characteristics, the flexure dimensions are adjusted to have  $\omega_n$  within the major spectrum of the floor vibrations below 30 Hz. The resulting dimension is  $L_{flex} = 40$  mm,  $h_{flex} = 0.3$  mm,  $w_{flex} = 104$  mm and  $n_{flex} = 4$  for  $\omega_n = 18.7$  Hz.

### 3.2. Flexure layout

Fig. 3(a) shows a 3D model of the mover, at the center of gravity (COG) of which a coordinate frame is attached. To vertically guide the mover, multiple flexures are used. As a layout, flexures can be asymmetrically attached in parallel to one side of the mover (e.g. only Flexure 1 and 2 in Fig. 3(a)). Although such a layout is commonly seen in optical disk drives [30], it creates a parasitic motion between the vertical ( $z_m$ ) and horizontal ( $y_m$ ) axes [31]. While the asymmetrical flexure layout is possible for AFM imaging, the horizontal parasitic motion is critical for high imaging resolution [32]. Although the parasitic motion can be compensated by using compound flexures [31], they require additional solid masses, which may create new mechanical resonances reducing the achievable closed-loop control bandwidth. Thus, for a high bandwidth, the four leaf-spring flexures are symmetrically aligned as shown in Fig. 3(a).

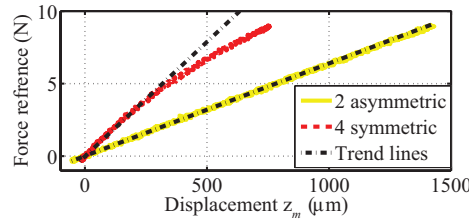


Figure 4: Measured relation of the mover’s vertical displacement and the force reference with trend lines. While the red dashed line is the results with the adopted flexure layout in Fig. 3(a), the yellow solid is with the asymmetrical layout using only Flexure 1 and 2 in Fig. 3(a) for comparison.

### 3.3. Stiffness variation and actuation range

The symmetrical layout compensating for the parasitic motion in Fig. 3(a) can cause a tensile force and deform the flexures, dependent on the mover’s vertical position. Because this force may increase the stiffness  $k$  of the Z axis, it is experimentally investigated by comparing the adopted symmetrical layout with an asymmetrical layout using only Flexure 1 and 2 in Fig. 3(a). For the experiments, the mover is vertically actuated by the two Lorentz actuators. While the given force is calculated from the actuators’ motor constant (7.2 N/A) and the amplifiers’ input, its vertical displacement from the neutral position under gravity is measured by a laser Doppler vibrometer (OFV534, Polytec, Irvine, USA). The AFM system is placed on an optical table for this characterization measurement to avoid floor vibrations.

Fig. 4 shows the results with trend lines indicating the slopes around the origin, where the direction of a positive force reference is the opposite of gravity. The asymmetrically aligned flexures for comparison (yellow solid line) follows its trend line well. In contrast, the adopted symmetrical alignment (red dashed line) shows a slope getting softer as the force reference increases because the pre-tension of the flexures due to gravity is relieved by lifting the mover upward. Note that if the actuators pull the mover downward, the tensile force increases, resulting in a larger stiffness  $k$ .

Because the variation of the stiffness  $k$  influences the vibration rejection performance, it is quantified for analysis (cf. Section 5.2). From the slope in Fig. 4,  $k$  is calculated as 15.8 kN/m at the origin, which is decreased by 47 % at 8.4 N. By adding a margin, the maximum variation (i.e. tolerance) is determined as  $\pm 60$  %. Notice that Fig. 4 demonstrates a Z-axis actuation of more than 700  $\mu\text{m}$ , which is about two orders of magnitude larger than typical commercial AFMs [6].

### 3.4. Over-actuation and frequency response

Taking an advantage of the multiple Lorentz actuators, over-actuation is used to prevent the Z actuation from exciting rotational modes for a high control bandwidth. Fig. 3(b) illustrates the concept, showing a cross-sectional view on the  $z_m - x_m$  plane in Fig. 3(a). The Lorentz coil 1 and 2 provide the actuation force  $F_1$  and  $F_2$ , respectively. They generate a torque  $\tau_y$  around the  $y_m$  axis

$$\tau_y = L_1 F_1 - L_2 F_2, \quad (2)$$

where  $L_1$  and  $L_2$  are the distances from coil 1 and 2 to the COG along the  $x_m$  axis, respectively. Since  $F_1$  and  $F_2$  are proportional to the respective amplifier reference  $u_{a1}$  and  $u_{a2}$ ,  $\tau_y$

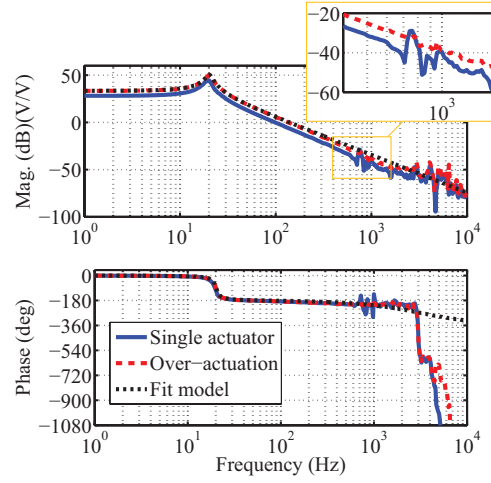


Figure 5: Measured Bode plot from the amplifier reference to the displacement sensor output  $y_d$ , and the simulated response of the fit model (10).

is zero with the following ratio

$$r_u = u_{a1}/u_{a2} = F_1/F_2 = L_2/L_1, \quad (3)$$

balancing the rotational mode by the over-actuation of the translational mode. Because of the symmetrical design ( $L_1 = L_2$ ),  $r_u$  is one for the AFM system.

For validation, Bode plots are measured from the current amplifiers' reference to the displacement sensor's output, as shown in Fig. 5. Because floor vibrations influence the frequency response, the AFM system is temporary moved onto an optical table. When only one actuator is used, resonance peaks are visible between 600 Hz and 1 kHz in the enlarged magnitude plot of Fig. 5. They are significantly reduced by the two actuators with  $r_u = 1$  for the over-actuation, demonstrating its effectiveness. The over-actuation renders the undesired mechanical modes uncontrollable [33]. Because these modes are stable, they can be neglected in feedback control design for a high control bandwidth.

## 4. System modeling

### 4.1. Lumped mass model

The lumped mass model of Fig. 2 is used to derive an analytical model of the AFM system. The actuation force of the Lorentz actuators are summed up as  $F$ , and the equation of motion about  $m$  is

$$m\ddot{z}_m + c(\dot{z}_m - \dot{z}_b) + k(z_m - z_b) = F. \quad (4)$$

Laplace transform of (4) gives

$$Z_m(s) = P_a(s)F(s) + P_t(s)Z_b(s), \quad (5)$$

using

$$P_a(s) = (ms^2 + cs + k)^{-1}, \quad P_t(s) = (cs + k)P_a(s), \quad (6)$$



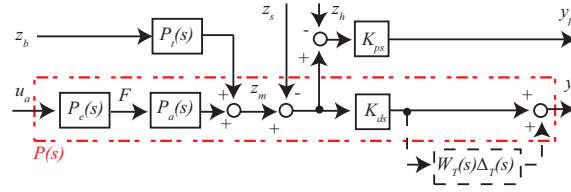


Figure 6: Block diagram of modeled system, where  $u_a$  ( $=u_{a1}=u_{a2}$ ) is the current amplifier reference with sample height  $z_h$ . The outputs of the probe and the displacement sensor are represented by  $y_p$  and  $y_d$ . Vibrations  $z_b$  and  $z_s$  are regarded as disturbances. The black dashed lines and block represent a model uncertainty.

where  $Z_m(s)$ ,  $Z_b(s)$  and  $F(s)$  are the Laplace transform of the mover position  $z_m$ , the fixed base position  $z_b$  and  $F$ , respectively. The transfer function  $P_t(s)$  from  $z_b$  to  $z_m$  is the (passive) transmissibility [10].

As the probe measures the distance between the mover and the sample surface, its output voltage  $y_p$  is given with its sensitivity  $K_{ps} = 1.56 \text{ V}/\mu\text{m}$  as follows

$$Y_p(s) = K_{ps}(Z_m(s) - Z_s(s) - Z_h(s)), \quad (7)$$

where  $Z_s(s)$ ,  $Z_h(s)$  and  $Y_p(s)$  are the Laplace transform of the sample stage position  $z_s$ , the sample height  $z_h$  and  $y_p$ , respectively. Similarly, the output voltage  $y_d$  of the displacement sensor is

$$Y_d(s) = K_{ds}(Z_m(s) - Z_s(s)), \quad (8)$$

where  $Y_d(s)$  is the Laplace transform of  $y_d$ , and  $K_{ds}$  is the displacement sensor's sensitivity  $0.2 \text{ V}/\mu\text{m}$ . Since both current amplifiers receive a common reference signal with  $r_u = 1$ , it is defined as  $u_a = u_{a1} = u_{a2}$ , and the transfer function  $P_e(s)$  from  $u_a$  to  $F$  is

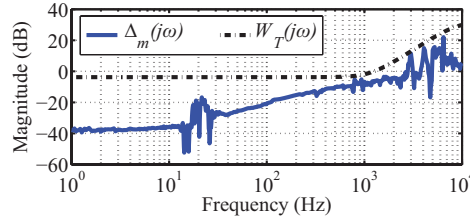
$$P_e(s) = \frac{F(s)}{U_a(s)} = 2K_a K_m \frac{1 - \frac{\tau}{2}s}{1 + \frac{\tau}{2}s}, \quad (9)$$

where  $U_a(s)$  is the Laplace transform of  $u_a$  with the Lorentz actuators' motor constant  $K_m = 7.2 \text{ N/A}$  and the current amplifiers' gain  $K_a = 200 \text{ mA/V}$ . The parameter  $\tau$  is a delay modeled by the first-order Pade approximation to capture a phase lag due to the electronics. By combining (5) - (9), the AFM system can be modeled as shown in Fig. 6. For control design, the transfer function  $P(s)$  from  $u_a$  to  $y_d$  is given by

$$P(s) = \frac{Y_d(s)}{U_a(s)} = \left( \frac{g}{\frac{s^2}{\omega_n^2} + 2\zeta \frac{s}{\omega_n} + 1} \right) \left( \frac{1 - \frac{\tau}{2}s}{1 + \frac{\tau}{2}s} \right), \quad (10)$$

where the gain  $g$  and the damping ratio  $\zeta$  are

$$g = \frac{2K_{ds}K_aK_m}{k}, \quad \zeta = \frac{c}{2\sqrt{km}}. \quad (11)$$

Figure 7: Multiplicative uncertainty  $\Delta_m(j\omega)$  and its upper bound  $W_T(s)$ .

#### 4.2. Parameter estimation

In the derived model (10), the stiffness  $k$  has a large variation of  $\pm 60\%$ , and the other parameters  $c$  and  $\tau$  are unknown. Thus, they are estimated together with a nominal value of  $k$ , based on the measured frequency response from  $u_a$  to  $y_d$  (i.e. the red dashed line in Fig. 5). The parameters  $k$ ,  $c$  and  $\tau$  are tuned such that the magnitude and the phase of the model (10) fit with the measured response. The fitting results with  $k = 13.8$  kN/m,  $c = 15.3$  N/(m/s), and  $\tau = 100$   $\mu$ s are shown by the black dotted line in Fig. 5. The first resonance at 20.2 Hz is well-modeled, validating the model (10). However, the high-frequency resonances are not captured to keep the model order low for a low-order feedback controller, which is desired for the implementation.

The stiffness  $k = 13.8$  kN/m is 15.5 % lower than the value measured in Section 3.2. This might result from a required reassembly of the AFM system for evaluation, and  $k$  is sensitive to the assembly precision. Note, however, that the 15.5 % variation is sufficiently smaller than the determined upper bound of  $\pm 60\%$ .

#### 4.3. Modeling error

Although the resonances beyond 2 kHz are not modeled, they are a factor limiting the achievable closed-loop control bandwidth. Thus, they are considered as a modeling error and quantified by the multiplicative uncertainty [34]

$$\Delta_m(j\omega) = |P_m(j\omega)/P(j\omega) - 1|, \quad (12)$$

where  $P_m(j\omega)$  represents the measured frequency response.

For control design, the upper bound of  $\Delta_m(j\omega)$  is approximated by a low-order transfer function  $W_T(s)$ , which is tuned to cover  $\Delta_m(j\omega)$  [34] as shown in Fig. 7. The resulting  $W_T(s)$  is

$$W_T(s) = 0.65 \frac{s^2/(2\pi \cdot 1150)^2 + 1.4s/(2\pi \cdot 1150) + 1}{s^2/(2\pi \cdot 9000)^2 + 1.4s/(2\pi \cdot 9000) + 1}. \quad (13)$$

The uncertainty with the upper bound is described as an additional loop in the block diagram of Fig 6, where  $\Delta_T(s)$  denotes any stable transfer function having a magnitude of one or less at any frequencies [35]. The upper bound  $W_T(s)$  increases at high frequencies due to the resonances at about 3 kHz and 5 kHz. In feedback control design, they restrict the achievable bandwidth for closed-loop stability because of the small gain theorem [35]. In contrast, the rotational modes compensated by the over-actuation below 1 kHz do not influence the pass band of  $W_T(s)$  and, consequently, do not limit the bandwidth.

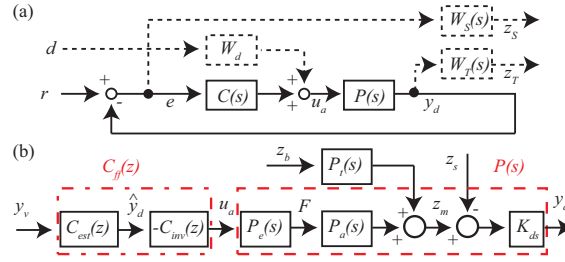


Figure 8: Control block diagrams for the design of (a) feedback controller  $C(s)$  and (b) feedforward controller  $C_{ff}(z)$ . The dashed-line blocks are weighting functions for the design of  $C(s)$ . The feedforward controller  $C_{ff}(z)$  consists of an error estimator  $C_{est}(z)$  and a plant inverse model  $C_{inv}(z)$  to cancel the vibrations  $z_b$  and  $z_s$ .

## 5. Control design

### 5.1. Feedback control design

Equation (7) implies that the sample height  $z_h$  can be measured by the probe without the vibrations of  $z_s$  and  $z_b$  when the mover tracks the sample stage (i.e.  $z_m = z_s$ ). This can be realized by feedback control using the displacement sensor signal  $y_d$ . The advantage of the configuration is that the vibration isolation performance is independent of the AFM probe, the sensitivity of which would be different for each probe [28].

For the feedback control design,  $H_\infty$  control synthesis [35] is used to guarantee stability with the modeling error  $\Delta_m(j\omega)$ , based on Fig. 8(a) with the plant model  $P(s)$  of (10). The signal  $r$  is the setpoint, and  $e$  is the sample tracking error. The modeling error  $\Delta_m(j\omega)$  is considered by  $W_T(s)$  used as the weighting function of the complementary sensitivity function  $T(s)$ , which is the transfer function from  $r$  to  $y_d$ . The vibration rejection performance can be determined by tuning the weighting function  $W_S(s)$  of the sensitivity function  $S(s)$ , which is the transfer function from  $r$  to  $e$ . The signal  $d$  weighted by a constant  $W_d$  is introduced to prevent the feedback controller  $C(s)$  from canceling the plant poles, which is needed to use the first mechanical resonance for vibration rejection [21].

The controller  $C(s)$  is obtained by minimizing the  $H_\infty$  norm of the transfer function from  $r$  and  $d$  to the weighted signal  $z_s$  and  $z_T$ . The weight  $W_d$  is adjusted to 0.1, which is sufficient to prevent the pole-zero cancellation, and  $W_S(s)$  is tuned to maximize its cross-over frequency under the condition that the minimized norm is less than one for robust stability [35]. The resulting  $W_S(s)$  and  $C(s)$  are

$$W_S(s) = 0.1 \frac{s + 2\pi \cdot 4100}{s + 2\pi \cdot 0.2}, C(s) = \frac{\sum_{i=0}^5 b_i s^{-i}}{\sum_{i=0}^5 a_i s^{-i}}, \quad (14)$$

where  $a_i$  and  $b_i$  are coefficients listed in Table 1.

### 5.2. Feedback control analysis

In this section, the effectiveness of the designed controller  $C(s)$  for the vibration isolation and rejection is investigated by taking the  $\pm 60\%$  stiffness variation into account. The

Table 1: Coefficients of the feedback controller  $C(s)$ 

$i$	0	1	2	3	4	5
$a_i$	1	4.85e05	9.38e10	2.75e15	2.85e19	1.19e19
$b_i$	2450	2.43e08	1.18e13	1.60e17	4.33e19	7.96e21

residual vibrations  $z_m - z_s$  of the closed-loop system with  $r=0$  are given by replacing  $U_a(s)$  by  $-C(s)Y_d(s)$  in Fig. 6 as follows

$$Z_m(s) - Z_s(s) = S(s)P_t(s)Z_b(s) - S(s)Z_s(s), \quad (15)$$

where the sensitivity function is  $S(s) = (1 + C(s)P(s))^{-1}$ .

Because  $S(s)$  dominates the rejection of  $z_b$  and  $z_s$  in (15), it is simulated by varying  $k$  from -60 % to 60 % in steps of 5 %, as shown by the black dash-dotted lines Fig. 9. Because the high gain of  $P(s)$  at  $\omega_n$  (Fig. 5) decreases  $S(s)$ , the simulation shows a notch around 20 Hz, clearly demonstrating the use of the first resonance for better rejection. As a result, the magnitude is smaller than -32 dB within the major spectrum of the floor vibrations below 30 Hz, which corresponds to the vibration rejection of 97 % or better dependent on the stiffness variation. More importantly, since the resonance contributes to the rejection,  $S(s)$  is always smaller than  $1/W_S(s)$  in Fig. 9, regardless of the stiffness variation. Consequently the closed-loop system satisfies the following condition of robust performance [35] against the stiffness variation

$$|W_S(j\omega)S(j\omega)| < 1 \quad \forall \omega. \quad (16)$$

The solid red line of Fig. 9 is the measured sensitivity function. It follows the trend of the simulation, validating the above discussions.

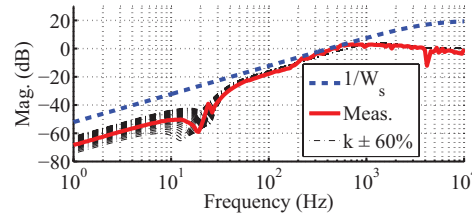


Figure 9: Sensitivity function  $S(s)$ . The red solid line shows the measured results while the blue dashed line is the inverse of the weighting function  $1/W_S(s)$  of  $S(s)$ . The black dash-dotted lines are simulated by changing  $k$  in a range of  $\pm 60$  %.

The rejection of  $z_b$  is determined by  $S(s)P_t(s)$  with feedback control. Thus, it is defined as the active transmissibility and simulated by varying  $k$  from -60 % to 60 % in steps of 5 % in comparison with the passive transmissibility  $P_t(s)$ . In Fig. 10,  $P_t(s)$  without feedback control shows the magnitude smaller than 0 dB beyond 40 Hz. This is the mechanical vibration isolation realized by the lowered stiffness  $k$ . However, the magnitude has a peak around 20 Hz because  $z_b$  excites the first resonance. In the case of the active transmissibility for AFM imaging, the peaks are perfectly eliminated by the notch of  $S(s)$  around 20 Hz, exhibiting a high vibration isolation of -32 dB or better in the entire frequency range, regardless of the stiffness variation. This means that 97 % or more of the vibrations  $z_b$  can be isolated.

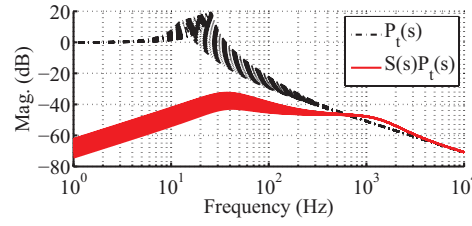


Figure 10: Simulated passive transmissibility  $P_t(s)$  and active transmissibility  $S(s)P_t(s)$  by changing  $k$  in a range of  $\pm 60\%$ .

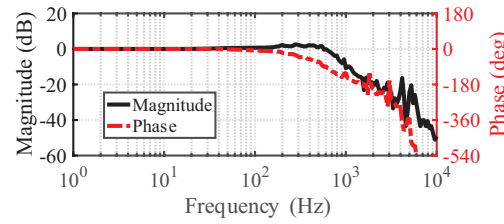


Figure 11: Measured complementary sensitivity function  $T(s)$ .

### 5.3. Achieved closed-loop control bandwidth

The closed-loop control bandwidth (-3 dB) is identified as 720 Hz by measuring the complementary sensitivity function  $T(s)$ , as shown in Fig. 11. Since this is 35 times higher than the first resonant frequency of 20.2 Hz, the AFM system overcomes the trade-off between the achievable actuation range (i.e. stroke) and the control bandwidth.

### 5.4. Feedforward control design

Since the vibration rejection of feedback control is restricted by the high mechanical resonances, feedforward control with the vibration sensor [12] is combined to cancel the transmitted vibrations for improvement. Feedforward control does not ideally introduce system instability, and it is easily combined with feedback control without modification [34].

Fig. 8(b) shows a block diagram of feedforward control. The objective is to cancel the vibrations  $z_b$  and  $z_s$  by means of the control input  $u_a$ , such that  $y_d$  stays zero. In order to do so, the feedforward controller  $C_{ff}(z)$  consists of an estimator  $C_{est}(z)$  and a plant inverse model  $C_{inv}(z)$ . The transfer function  $C_{est}(z)$  estimates  $y_d$  from the vibration sensor output  $y_v$ . Based on the estimated value  $\hat{y}_d$ ,  $C_{inv}(z)$  generates  $u_a$  for vibration cancellation. The design of the controller is presented below.

#### 5.4.1. Design of estimator

Because  $C_{est}(z)$  is influenced by unknown modes of the laboratory table,  $y_v$  and  $y_d$  are related by the following general discrete black-box model [36]

$$y_d(t_d) = C_{est}(q)y_v(t_d) + H_{est}(q)v(t_d), \quad (17)$$

using

$$C_{est}(q) = \frac{q^{-n_k}B_p(q)}{A_p(q)F_p(q)}, \quad H_{est}(q) = \frac{C_p(q)}{A_p(q)D_p(q)}, \quad (18)$$

where  $A_p(q)$ ,  $B_p(q)$ ,  $C_p(q)$ ,  $D_p(q)$  and  $F_p(q)$  are polynomials of the forward shift operator  $q$ . The white noise, delay and discrete time sequence are represented by  $v(t_d)$ ,  $n_k$  and  $t_d$ , respectively.

To determine  $n_k$  and the polynomials, a parametric system identification [36, 37] is applied. While feedback control is inactive,  $y_v$  and  $y_d$  are recorded, and the data are divided into two sets for cross validation. With the first data set, the MATLAB command *polyest* is used to obtain the polynomials and  $n_k = 2$ . Using the second data set, the cross correlation of  $y_v$  and the residuals [37]

$$\varepsilon_{est}(t_d) = H_{est}^{-1}(q) \{y_d(t_d) - C_{est}(q)y_v(t_d)\}, \quad (19)$$

is calculated for the validation. The resulting correlation is within the 99% confidence interval. Thus,  $y_v$  and  $\varepsilon_{est}$  are uncorrelated, implying that the dynamics between  $y_v$  and  $y_d$  are well-captured by  $C_{est}(q)$  to generate  $\hat{y}_d$ .

#### 5.4.2. Design of plant inverse model

To generate  $u_a$  from  $\hat{y}_d$ , the inverse of the plant model  $P(s)$  in (10) is approximated and discretized by the bilinear transformation [34] as follows

$$C_{inv}(z) = \frac{z^2}{g} \left( \frac{\frac{s^2}{\omega_n^2} + 2\zeta \frac{s}{\omega_n} + 1}{\frac{s^2}{\omega_c^2} + \sqrt{2} \frac{s}{\omega_c} + 1} \right) \bigg|_{s=\frac{2}{T_s} \frac{z-1}{z+1}}, \quad (20)$$

where  $T_s$  is the sampling time of  $50 \mu s$ , and the time advance  $z^2$  results from the delay  $\tau = 100 \mu s$  of  $P(s)$ . A second-order low-pass filter is incorporated to have  $C_{inv}(z)$  proper. Its cut-off frequency  $\omega_c$  is set to 1 kHz, sufficiently higher than the measured floor vibrations.

#### 5.4.3. Overall feedforward control design

From (18) and (20), by replacing  $q$  by  $z$ , the feedforward controller  $C_{ff}(z) = -C_{inv}(z)C_{est}(z)$  is given by

$$C_{ff}(z) = \frac{-B_p(z)}{gA_p(z)F_p(z)} \left( \frac{\frac{s^2}{\omega_n^2} + 2\zeta \frac{s}{\omega_n} + 1}{\frac{s^2}{\omega_c^2} + \sqrt{2} \frac{s}{\omega_c} + 1} \right) \bigg|_{s=\frac{2}{T_s} \frac{z-1}{z+1}}, \quad (21)$$

using the polynomials

$$\begin{aligned} A_p(z) &= 1 - 1.843z^{-1} + 0.505z^{-2} + 0.521z^{-3} - 0.183z^{-4}, \\ B_p(z) &= (-3.92 + 8.61z^{-1} - 4.69z^{-2}) \times 10^{-8}, \\ F_p(z) &= 1 - 0.912z^{-1}, \end{aligned} \quad (22)$$

where the time advance of  $C_{inv}(z)$  cancels the delay of  $C_{est}(z)$ . Since the parameters  $g$ ,  $\zeta$  and  $\omega_n$  are influenced by the variation of the stiffness  $k$ , their values are tuned at the implementation. As presented in the next section, the controller successfully cancels the vibrations with the geophone on the table. However, if its vibration measurement is interfered by the table's modes and the Z-axis actuation, the geophone may have to be relocated (e.g. directly onto the floor).



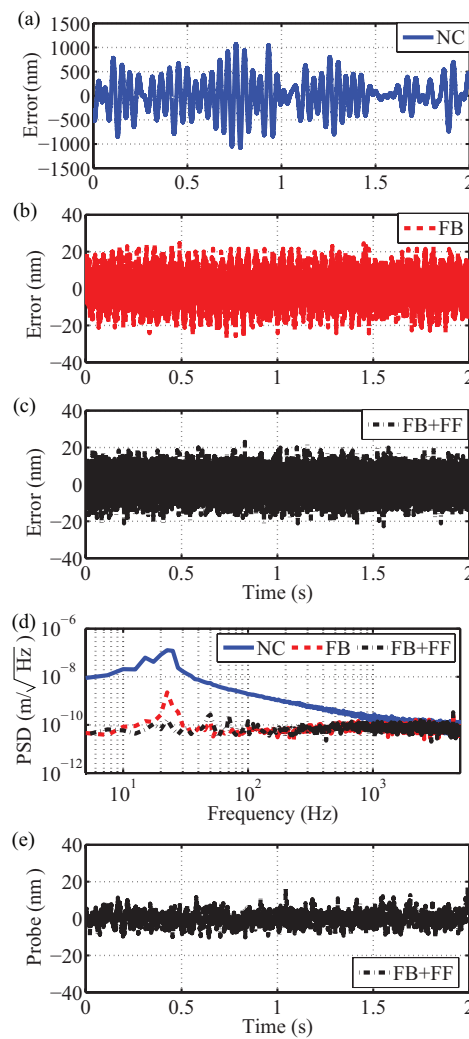


Figure 12: Measured tracking error  $e$  (a) when no control is applied, (b) when only the feedback controller is turned on, and (c) when both feedback and feedforward controllers are turned on. The plot (d) is their PSD. The graph (e) shows the measured AFM probe signal  $y_p$  while both feedback and feedforward controllers are active without scanning the sample.

## 6. Experimental results

To evaluate the AFM system in the vibrational environment (cf. Section 2) without external vibration isolation, experiments are carried out, when no control is applied (NC), when only the feedback controller is turned on (FB), and when both feedback and feedforward controllers are active (FB+FF).

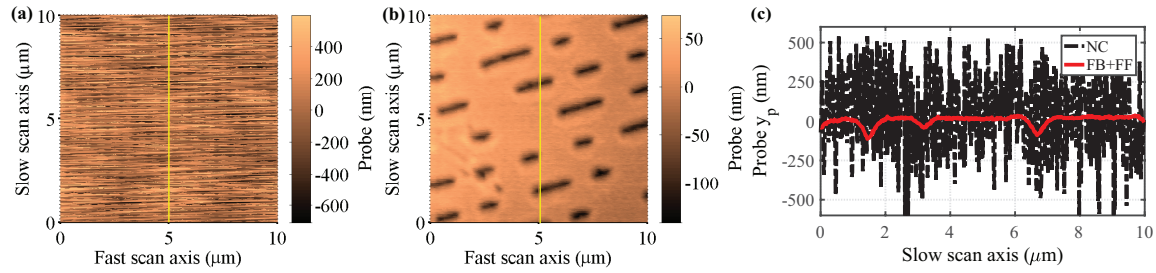


Figure 13: Experimental AFM images of CD-ROM (a) when no control is applied, and (b) when both feedback and feedforward controllers are active. The yellow lines in the images represent data sets for (c) single line profiles.

### 6.1. Vibration isolation performance

While the setpoint  $r$  is set to a constant, the sample tracking error  $e$  is recorded, as shown in Fig. 12. Only when no control is applied to the Lorentz actuators, the mean of  $e$  is eliminated for evaluation, as shown in Fig. 12(a), where the vibrations result in a large error of about  $\pm 1000$  nm. However, the feedback controller suppresses the error to approximately within  $\pm 20$  nm (Fig. 12(b)). It is further decreased by the feedforward controller in Fig. 12(c).

The spectral density in Fig. 12(d) shows that the feedback controller suppresses the vibrations by two decades of magnitude, and the residual vibrations between 10 Hz and 30 Hz are successfully eliminated by the feedforward controller. Particularly at 23 Hz, a vibration peak of  $128 \text{ nm}/\sqrt{\text{Hz}}$  is visible without control, which is decreased by 98.3 % to  $2.24 \text{ nm}/\sqrt{\text{Hz}}$  with the feedback controller and by 99.9 % to  $0.163 \text{ nm}/\sqrt{\text{Hz}}$  with the feedback and feedforward controllers. The RMS error is calculated from the data in Fig. 12, resulting in 378 nm without control, 7.18 nm with the feedback controller and 6.05 nm with both feedback and feedforward controllers. Overall, the AFM system eliminates 98.4 % of the vibrations by using the feedback and feedforward controllers. Due to the high vibration rejection, the achieved error (6.05 nm) is close to the displacement sensor's noise level (5.88 nm).

For further evaluation, the AFM probe is engaged with a sample without XY scanning, and its signal  $y_p$  is measured as shown in Fig. 12(e) while both feedback and feedforward controllers are active. The RMS value of  $y_p$  is 3.54 nm and contains the probe's measurement noise of 1.17 nm. The signal  $y_p$  also contains the vibrations due to the displacement sensor's noise, which can be estimated as 1.1 nm from its PSD ( $0.042 \text{ nm}/\sqrt{\text{Hz}}$ ) and the -3 dB Z-axis bandwidth (720 Hz). Therefore, a displacement sensor with smaller noise may be necessary dependent on samples. In summary, the AFM system successfully isolates and rejects floor vibrations to a nanometer level for AFM imaging in the next section.

### 6.2. AFM imaging

For AFM imaging, the pits of a CD-ROM are used as the sample. The reflective coating of the disk is stripped from the polycarbonate layer. The exposed polycarbonate surface has hollow pits of  $0.50 \mu\text{m}$  width, and the data tracks have a distance of  $1.6 \mu\text{m}$  [38]. The XY scanner is used for raster scanning with a triangular signal of 5 Hz.

The probe signal  $y_p$  is recorded at 10 kHz, and the mean of the data set is removed to generate AFM images ( $500 \times 500$  pixels), as shown in Fig. 13. Without control in Fig. 13(a),

no meaningful features are visible due to floor vibrations. When the feedback and feedforward controllers are activated in Fig. 13(b), the CD-ROM is imaged, clearly resolving the pits and tracks. The single line profile along the slow scan axis in Fig. 13(c) shows a smooth line with the controllers rejecting the vibrations for the imaging of the nanoscale features.

Overall, the experimental results successfully demonstrate the integration of vibration isolation with the vertical tracking of the sample surface in AFM instrumentation by means of the low-stiffness flexure-guided Lorentz actuators.

## 7. Conclusion

Vibration isolation is integrated in an AFM by using flexure-guided Lorentz actuators for the probe's Z-axis actuation. Mechanically decreasing the vibrations transmitted to the probe, the Z-axis actuators have a low stiffness between the mover and stator with the first resonance at 20.2 Hz. The displacement sensor measures the mover-sample distance as the residual vibrations, and they are rejected by the feedback controller. By ensuring a sufficient frequency band between the first and higher resonances, the closed-loop system achieves a high control bandwidth of 720 Hz, which is 35 times higher than the first resonant frequency. Consequently, the Z-axis actuators are no longer trapped in the stroke-bandwidth trade-off, demonstrating a movement of more than 700  $\mu\text{m}$ . By utilizing the first resonance and combining feedforward control, the AFM system is able to reject 98.4 % of the vertical vibrations. As a result, the AFM system is operational without external vibration isolation, as successfully demonstrated by imaging the pits and tracks of a CD-ROM in a vibrational environment.

## Acknowledgments

The authors would like to thank Mr. Daniel Neyer, Mr. Stefan Pirker and Dr. Juergen Steininger for electronics development and fruitful discussions. This work has been supported in part by the Austrian Research Promotion Agency (FFG) under project number 836489.

- [1] G. Binnig, C. F. Quate, C. Gerber, Atomic force microscope, *Phys. Rev. Lett.* 56 (1986) 930–933. doi:10.1103/PhysRevLett.56.930.
- [2] P. Eaton, P. West, *Atomic Force Microscopy*, Oxford University Press, 2010.
- [3] H. Amick, D. H. Sturz, E. E. Ungar, *Vibration control design of high technology facilities, Sound and Vibration* - (1990) 20–27.
- [4] G. Schitter, A. Stemmer, Eliminating mechanical perturbations in scanning probe microscopy, *Nanotechnology* 13 (5) (2002) 663–665. doi:10.1088/0957-4484/13/5/324.
- [5] J. H. Kindt, G. E. Fantner, J. A. Cutroni, P. K. Hansma, Rigid design of fast scanning probe microscopes using finite element analysis, *Ultramicroscopy* 100 (34) (2004) 259–265. doi:10.1016/j.ultramic.2003.11.009.
- [6] H. Barnard, C. Randall, D. Bridges, P. K. Hansma, The long range voice coil atomic force microscope, *Review of Scientific Instruments* 83 (2) (2012) 023705. doi:10.1063/1.3683235.

- [7] Q. Wang, Y. Hou, J. Wang, Q. Lu, A high-stability scanning tunneling microscope achieved by an isolated tiny scanner with low voltage imaging capability, *Review of Scientific Instruments* 84 (11) (2013) 113703. doi:10.1063/1.4829716.
- [8] C. Kim, J. Jung, W. Youm, K. Park, Design of mechanical components for vibration reduction in an atomic force microscope, *Review of Scientific Instruments* 82 (3) (2011) 035102. doi:10.1063/1.3531948.
- [9] H. Amick, M. Gendreau, T. Busch, C. Gordon, Evolving criteria for research facilities I: vibration, in: *Proc. SPIE* 5933, Vol. 5933, 2005, p. 593303. doi:10.1117/12.617970.
- [10] R. Munnig Schmidt, G. Schitter, A. Rankers, J. van Eijk, *The Design of High Performance Mechatronics*, 2nd Edition, Delft University Press, 2014.
- [11] R. Brincker, T. L. Lago, P. Andersen, C. Ventura, Improving the classical geophone sensor element by digital correction, in: *Conference and Exposition on Structural Dynamics*, 2005, p. 9.
- [12] G. Balik, B. Caron, J. Allibe, A. Badel, J.-P. Baud, L. Brunetti, G. Deleglise, A. Jeremie, R. Le Breton, S. Vilalte, Sub-nanometer active seismic isolator control, *Journal of Intelligent Material Systems and Structures* 24 (15) (2013) 1785–1795. doi:10.1177/1045389X13500571.
- [13] M. Thier, R. Saathof, A. Sinn, R. Hainisch, G. Schitter, Six degree of freedom vibration isolation platform for in-line nano-metrology, *IFAC-PapersOnLine* 49 (21) (2016) 149–156. doi:10.1016/j.ifacol.2016.10.534.
- [14] T. Nishino, E. Ikemoto, K. Kogure, Application of atomic force microscopy to observation of marine bacteria, *Journal of Oceanography* 60 (2) (2004) 219–225. doi:10.1023/B:JOCE.0000038328.54339.e4.
- [15] W. Xin, Y. Junping, F. Xiaohong, An AFM observation on fossil cytoplasm, *Acta Geologica Sinica* 82 (6) (2008) 1141–1145. doi:10.1111/j.1755-6724.2008.tb00714.x.
- [16] A. J. Fleming, Nanopositioning system with force feedback for high-performance tracking and vibration control, *IEEE/ASME Transactions on Mechatronics* 15 (3) (2010) 433–447. doi:10.1109/TMECH.2009.2028422.
- [17] Y. K. Yong, S. O. R. Moheimani, B. J. Kenton, K. K. Leang, Invited review article: High-speed flexure-guided nanopositioning: Mechanical design and control issues, *Review of Scientific Instruments* 83 (12) (2012) 121101. doi:10.1063/1.4765048.
- [18] A. W. Sparks, S. R. Manalis, Atomic force microscopy with inherent disturbance suppression for nanostructure imaging, *Nanotechnology* 17 (6) (2006) 1574–1579. doi:10.1088/0957-4484/17/6/007.
- [19] C. Kim, J. Jung, K. Park, Note: Vibration reduction control of an atomic force microscope using an additional cantilever, *Review of Scientific Instruments* 82 (11) (2011) 116102. doi:10.1063/1.3660776.

- [20] A. J. Fleming, A review of nanometer resolution position sensors: Operation and performance, *Sensors and Actuators A: Physical* 190 (0) (2013) 106–126. doi:10.1016/j.sna.2012.10.016.
- [21] S. Ito, G. Schitter, Comparison and classification of high-precision actuators based on stiffness influencing vibration isolation, *IEEE/ASME Transactions on Mechatronics* 21 (2) (2016) 1169–1178. doi:10.1109/TMECH.2015.2478658.
- [22] S. Ito, J. Steininger, G. Schitter, Low-stiffness dual stage actuator for long range positioning with nanometer resolution, *Mechatronics* 29 (2015) 46–56. doi:10.1016/j.mechatronics.2015.05.007.
- [23] S. Ito, S. Unger, G. Schitter, Vibration isolator carrying atomic force microscopes head, *Mechatronics* 44 (2017) 32–41. doi:10.1016/j.mechatronics.2017.04.008.
- [24] G. Schitter, K. J. Astrom, B. E. DeMartini, P. J. Thurner, K. L. Turner, P. K. Hansma, Design and modeling of a high-speed afm-scanner, *IEEE Transactions on Control Systems Technology* 15 (5) (2007) 906–915. doi:10.1109/TCST.2007.902953.
- [25] T. Mariani, C. Frediani, C. Ascoli, A three-dimensional scanner for probe microscopy on the millimetre scale, *Applied Physics A* 66 (1998) S861–S866. doi:10.1007/s003390051257.
- [26] W. Youm, J. Jung, S. Lee, K. Park, Control of voice coil motor nanoscanners for an atomic force microscopy system using a loop shaping technique, *Review of Scientific Instruments* 79 (1) (2008) 013707. doi:10.1063/1.2829990.
- [27] M. Baranwal, R. S. Gorugantu, S. M. Salapaka, Robust atomic force microscopy using multiple sensors, *Review of Scientific Instruments* 87 (8) (2016) 083704. doi:10.1063/1.4960714.
- [28] T. Akiyama, U. Staufer, N. F. de Rooij, P. Frederix, A. Engel, Symmetrically arranged quartz tuning fork with soft cantilever for intermittent contact mode atomic force microscopy, *Review of Scientific Instruments* 74 (1) (2003) 112–117. doi:10.1063/1.1523631.
- [29] S. Ito, F. Cigarini, S. Unger, G. Schitter, Flexure design for precision positioning using low-stiffness actuators, in: *IFAC Symposium on Mechatronic Systems (IFAC-PapersOnLine)*, Vol. 49, 2016, pp. 200–205. doi:10.1016/j.ifacol.2016.10.548.
- [30] B. Zhang, J. Ma, L. Pan, X. Cheng, H. Hu, Y. Tang, Magnetic circuit design for six-wire suspension type actuator in a super multi-optical pickup, *IEEE Transactions on Magnetics* 44 (5) (2008) 598–604. doi:10.1109/TMAG.2008.918045.
- [31] H. Soemers, *Design Principles for Precision Mechanisms*, T-Point Print, 2011.
- [32] S. Ito, D. Neyer, S. Pirker, J. Steininger, G. Schitter, Atomic force microscopy using voice coil actuators for vibration isolation, in: *IEEE International Conference on Advanced Intelligent Mechatronics*, 2015, pp. 470–475. doi:10.1109/AIM.2015.7222578.

- [33] M. J. C. Ronde, M. G. E. Schneiders, E. J. G. J. Kikken, M. J. G. van de Molengraft, M. Steinbuch, Model-based spatial feedforward for over-actuated motion systems, *Mechatronics* 24 (4) (2014) 307–317. doi:10.1016/j.mechatronics.2013.09.010.
- [34] T. Yamaguchi, M. Hirata, C. Pang, High-Speed Precision Motion Control, Taylor & Francis, 2011.
- [35] S. Skogestad, I. Postlethwaite, Multivariable Feedback Control, John Wiley, 2005.
- [36] L. Ljung, System Identification, Prentice Hall PTR, 1999.
- [37] L. Ljung, T. Glad, Modeling of Dynamic Systems, Prentice Hall, 1994.
- [38] K. Clements, Understanding and Servicing CD Players, Newnes, 1994.